Comparing 3D and 2D CFD for Mars Helicopter Ingenuity Rotor Performance Prediction

Witold J. F. Koning,[1,*] Brian G. Allan,[2,†] Ethan A. Romander,[1,‡] Wayne Johnson[1,§]

[1] NASA Ames Research Center, Moffett Field, California 94035
[2] NASA Langley Research Center, Hampton, Virginia 23681

Single and coaxial rotor performance simulations for the Mars Helicopter Ingenuity rotor are performed for representative Mars atmospheric conditions. Analyses are presented using both a high-fidelity 3D CFD model of the rotor and 2D CFD models of the airfoil sections for comprehensive analyses that use CAMRADII (Comprehensive Analytical Model of Rotorcraft Aerodynamics and Dynamics). When available, the airfoil performance calculations are generated using a numerical approach identical to that used in the high-fidelity 3D model, allowing for a direct comparison between the approaches. Experimental data from a validation campaign to explore higher thrust from an Ingenuity rotor is provided to substantiate a discussion on the simulation fidelity required for both coaxial and single rotor performance predictions. The data is in support of the Sample Recovery Helicopter (SRH) element that serves as the primary backup for tube retrieval as part of the Mars Sample Return (MSR) Campaign. Insights on modeling turbulence at low Reynolds numbers and its influence on the rotor figure of merit are discussed. Key rotor performance metrics are compared. A detailed investigation into differences between 2D and 3D rotor performance predictions, spanwise loading, and rotor stall behavior is included.

Nomenclature

a = speed of sound, m/s
A = rotor disk area, m^2
c = chord, m
C = section aerodynamic axial (chord) force, N/m
c_c = sectional axial force coefficient, $C/(0.5\rho V^2 c)$
c_n = sectional normal force coefficient, $N/(0.5\rho V^2 c)$
C_P = rotor power coefficient, $P/(\rho A(\Omega R)^3)$
C_T = rotor thrust coefficient, $T/(\rho A(\Omega R)^2)$
FM = hover figure of merit, $T\sqrt{T/(2\rho A)}/P$
M = blade section Mach number
N = section aerodynamic normal force, N/m
P = rotorcraft power, W
r = rotor radial coordinate, m
R = gas constant, $\mathrm{m/(s^2 K)}$; rotor radius, m
Re = chord-based Reynolds number, $\rho V c/\mu$
t = time, s
t_{phys} = physical time, tc/V
T = temperature, K; rotor thrust, N
V = section resultant velocity, m/s
y^+ = dimensionless wall distance
α = angle of attack, deg
γ = specific heat ratio
θ = rotor collective angle, deg
μ = dynamic viscosity, $\mathrm{Ns/m^2}$
ψ = rotor azimuth angle, deg
ρ = density, $\mathrm{kg/m^3}$
σ = rotor solidity (thrust-weighted)
Ω = rotor rotational speed, rad/s

Subscripts
c = chord-based
tip = tip-based

* Aerospace Engineer, Aeromechanics Branch, and Science and Technology Corporation; witold.koning@nasa.gov.
† Aerospace Engineer, Flow Physics and Control Branch; brian.g.allan@nasa.gov.
‡ Aerospace Engineer, Aeromechanics Branch; ethan.romander@nasa.gov.
§ Aerospace Engineer, Aeromechanics Branch; wayne.johnson@nasa.gov.

I. Introduction

The Mars Helicopter *Ingenuity* made history in April 2021 by being the first aircraft in history to make a powered, controlled flight on another planet [1]. The National Aeronautics and Space Administration (NASA) Jet Propulsion Laboratory (JPL) designed the Mars Helicopter (MH) in collaboration with AeroVironment Inc. and other NASA centers. Helicopter design for operation on Mars presents challenges generally not encountered for terrestrial designs [2,3]: the low atmospheric density on Mars, the communication delays to Earth, and the space environment (thermal, radiation) are some of the key factors rapidly increasing design complexity. The former is of particular importance to flight in the Martian atmosphere and presents many new challenges for the vehicle flight dynamics [4–7] and aerodynamics [8,9].

Pioneering work on rotorcraft planetary exploration was performed by Young et al. [10–13] and Datta et al. [14]. Early development of Ingenuity started in 2013 and an early conceptual design was published the following year [15]. Ingenuity features a coaxial rotor with a 1.21 m rotor diameter and a total vehicle mass of 1.8 kg. The helicopter relies on solar cells and a battery system for power, demonstrating flight endurance of up to ~170 seconds that is conducted fully autonomously due to the communication delay between Earth and Mars. The rotor design features two counter-rotating, hingeless, two-bladed rotors [4].

Recently, the Sample Recovery Helicopter (SRH) element was announced [16], serving as the primary backup for soil sample tube retrieval as part of the Mars Sample Return (MSR) Campaign.[*] The MSR program aims to bring Mars materials back to Earth for the first time. Under current planning, a Sample Retrieval Lander (SRL) will bring a small rocket, the Mars Launch System (MLS) and two Sample Recovery Helicopters to Mars in 2030. The SRH mission leverages on the design heritage of Ingenuity: each helicopter consists of an Ingenuity-like rotorcraft with the addition of ground mobility and a manipulator. An experimental validation campaign to explore higher thrust from an Ingenuity-like rotor was performed by the Jet Propulsion Laboratory (JPL) with support from AeroVironment, Inc. [16].

The design of the Ingenuity rotor was performed by AeroVironment, Inc. using their PROP code and Mark Drela's XROTOR [2,3,17]. Additional aerodynamic analyses were completed on Ingenuity's rotor blade geometry in 2018 using 2D Computational Fluid Dynamics (CFD) to generate airfoil tables to drive the Comprehensive Analysis (CA) code CAMRAD II [8,9]. CAMRAD II is a CA tool for rotorcraft [18] and has undergone extensive correlation of performance and loads measurements on rotorcraft, including coaxial rotors [19]. Furthermore, for a select number of cases, high-fidelity 3D CFD was used to predict rotor performance.

Given the heavy usage of CA to guide the design of Ingenuity, understanding the differences in rotor performance predictions between 2D and 3D CFD aerodynamic modeling is key, as this can affect critical rotor performance parameters including accuracy of rotor peak figure of merit (FM) predictions, rotor stall behavior, and compressibility effects. Understanding where rotor performance discrepancies can appear, identifying what the role of the numerical approach is, and comparing the influence of strict 2D versus full 3D modeling are key to better understanding of CA-based rotor performance predictions at compressible low Reynolds number conditions.

The goal of this work is to compare 2D CFD as aerodynamic inputs for comprehensive analyses to 3D CFD of the isolated Ingenuity rotor in hover. Data from the recent experimental validation campaign is provided, both for coaxial and single rotor configurations, to further allow the comparison with analytical methods. Rotor hover performance metrics, sectional and spanwise performance comparisons, and stall predictions are compared and investigated.

II. Experimental Data

To support the increased liftoff mass, an increased blade loading and increased tip Mach numbers, amongst others, are parameters being considered for SRH [16]. This prompted an experimental validation campaign to increase blade loading and tip Mach number to validate predicted increases in rotor thrust from an Ingenuity rotor. A coaxial test campaign and a single rotor test were performed to identify stall characteristics and drag divergence effects, respectively, at representative Mars atmosphere conditions. The experiments were conducted at the JPL Space Simulator (JPLSS) using CO_2 as the driving gas. The approximate operating conditions during the experimental campaigns are shown in Table 1, next to sea-level standard (SLS) conditions for Earth.

Table 1 Approximate JPLSS Test Conditions

Variable	Earth (SLS)	EDM1	TRT
Density, ρ (kg/m^3)	1.225	*Varying*	0.0100
Temperature, T (K)	288.20	293.15	293.15
Gas constant, R (m^2/s^2/K)	287.10	188.9	188.9
Specific heat ratio, γ	1.400	1.289	1.289
Dynamic viscosity, μ (N·s/m^2)	$1.750 \cdot 10^{-5}$	$1.46 \cdot 10^{-5}$	$1.46 \cdot 10^{-5}$
Speed of sound, a (m/s)	340.35	267.17	267.17

The Ingenuity design uses a 25% rotor thrust margin to account for uncertainties in predicting rotor (stall) performance in the Mars atmosphere. Next to that, the highest hover tip Mach number flown on Mars is approximately $M_{tip} = 0.72$, leaving room for improved performance if compressibility effects prove to be acceptable.

Further understanding of rotor performance predictive capabilities possibly allow for more accurate risk quantification and increased performance figures in future Mars helicopter designs. Experimental data from the two tests are included to provide context to the two approaches to rotor performance predictions presented herein.

---

[*] The decision to implement Mars Sample Return will not be finalized until NASA's completion of the National Environmental Policy Act (NEPA) process. This document is being made available for information purposes only.

A. The Transonic Rotor Test (TRT)

A single Ingenuity rotor was used to investigate possible increases in tip Mach number. While higher tip speeds could improve both dimensional thrust and efficiency (due to Reynolds number increases), decreasing the tip speed margin necessitates that compressibility effects and eventually drag divergence are well characterized. Figure 1 shows the experimental setup of the TRT, showing the bottom mounted motor ('M'), the single rotor and the support structure on top.
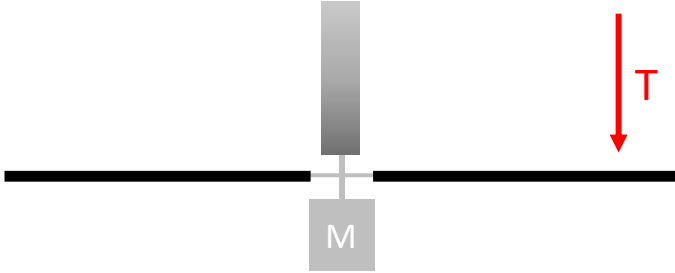
Figure 1 The schematic experimental setup for the TRT test in the JPL Space Simulator.

The TRT primary rotor performance measurements are rotor thrust and torque (from which shaft power was derived). Ingenuity's highest hover tip Mach number is $M_{tip} = 0.72$. The Transonic Rotor Test (TRT) showed that Ingenuity's rotor can spin up to $M_{tip} = 0.85$, corresponding to $M_{tip} = 0.77$ in hover when taking cruise speed into consideration. The ground system equipment (GSE) prevented testing at higher Mach numbers. The tip Mach numbers and corresponding rotor RPM values in the TRT are summarized in Table 2.

Table 2 TRT Test Conditions

TRT condition	1	2	3	4	5
M_{tip}	0.65	0.70	0.75	0.80	0.85
RPM	2,740	2,950	3,160	3,375	3,585

B. The Engineering Design Model 1 Test Campaign

The Ingenuity Engineering Design Model 1 (EDM1) was used to perform several tests to investigate the (coaxial) rotor stall behavior in the EDM1 test campaign. Determining the usable thrust was key in evaluating current capabilities in simulating rotor performance. Figure 2 shows the experimental setup of the EDM1 test campaign in the JPLSS, showing the inverted Ingenuity airframe (landing legs, body and solar panel), the coaxial rotor, and the support arm on top.

The EDM1 campaign primary rotor performance measurements are system total thrust and estimated mechanical power of each motor. Testing of only one motor at a time and measurement of electrical power of the motor and motor torque allowed for computation of motor efficiency which allowed for an estimated mechanical power calculation of each rotor during the coaxial tests.

The campaign found stall at lower collective than initially expected from current best modeling practices. Qualitatively, the onset of stall occurred in a gradual build up ('soft') rather than immediate. The four rotor operating conditions are summarized in Table 3.
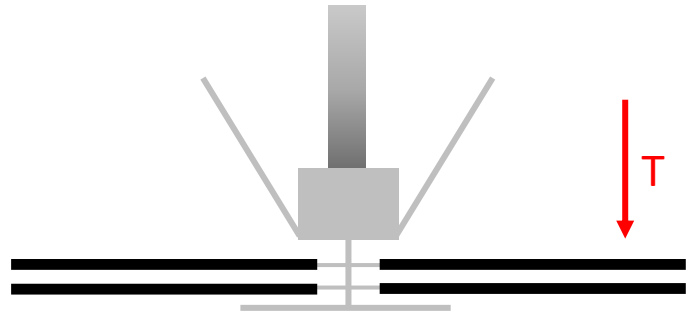

Figure 2 The schematic experimental setup for the EDM1 test campaign in the JPL Space Simulator.

Table 3 EDM1 Test Campaign Conditions

EDM1 condition	1	2	3	4
Density, ρ (kg/m^3)	0.0100	0.0185	0.0185	0.0300
M_{tip}	0.52	0.48	0.60	0.48
RPM	2,200	2,043	2,550	2,043

III. Numerical Approach

Airfoil and rotor performance for all CFD simulations are obtained using structured grids and solved using the implicit, compressible Navier-Stokes solver OVERFLOW 2.3d [20,21]. Inviscid fluxes are computed using the HLLC or HLLE++ flux schemes with a 5th-order WENOM upwind reconstruction approach for high spatial accuracy with low numerical dissipation [22]. Viscous fluxes are computed using second-order central differencing, as are grid metric terms. Time advance uses a second-order backward differencing scheme, with a dual time-stepping approach as described in Refs. [23,24].

CFD analyses for Ingenuity rotor conditions are complex because the modeling of turbulence at low Reynolds numbers is not trivial. A computationally efficient, Reynolds-Averaged Navier-Stokes (RANS) method is the only affordable option for airfoil table generation (which requires approximately 1,500 simulations per set of C81 tables) and also for 3D rotating blade CFD analyses. However, RANS approaches require special attention when modeling transition and turbulence, particularly at low Reynolds numbers.

A 'fully turbulent' approach was initially evaluated but is not advised because the Reynolds numbers are outside of the range of where the model should be used. The AFT2017-b transition model [25] provided good comparison to experimental test data at earlier representative conditions in the Space Simulator at the Jet Propulsion Laboratory (JPL) [8].

A later study [26] showed satisfactory correlation for Eppler 387 airfoil performance at low Reynolds numbers to experimental data when modeling laminar Unsteady Navier-Stokes (UNS) equations, meaning no turbulence model is employed. The study showed that mean behavior of unsteady Laminar Separation Bubbles (LSB) can be captured accurately using laminar UNS [26], and transition to turbulence was governed by a separated shear layer instability resulting in the shedding of large-scale coherent vortices, resulting in reattachment of the mean flow only.

Similar shear layer instabilities are observed in the sectional simulations for the Ingenuity rotor performance model [8], alluding to similar mechanisms at play and the relative importance of large-scale coherent motion, when compared to small-scale turbulence.

A. 2D Aerodynamic Airfoil Performance Simulations

CA conventionally uses sectional airfoil performance organized in C81 lookup tables for angle of attack-Mach combinations to model the rotor performance. Because the Ingenuity airfoil geometry was new and the aerodynamic environment unique, no such tables existed in 2018 before the first rotor model was generated. For this reason, 2D CFD was used to generate airfoil performance tables in C81 format at three representative Mars atmospheric conditions [8,9]. The eight radial stations at which the current calculations are performed are identical to those found in Ref. [8].

All airfoil surfaces are subjected to a no-slip adiabatic boundary condition and the far field boundaries are modeled using a freestream characteristic boundary condition. A 'quick start' [27] procedure is performed by using a relatively coarse physical timestep (the time it takes the freestream velocity to travel one chord length) $t_{phys} = 0.16$ and forcing only a 1-order drop in subiteration residual until the freestream has passed at least the entire domain. Subsequently, the physical timestep is reduced to $t_{phys} = 0.0025$ and subiterations are continued until three orders of subiteration convergence are achieved. After 25 passes of the flow over the chord, the following 50 airfoil flow passes are used to extract a meaningful mean of the unsteady flow.

The CA model for Ingenuity's rotor in hover is set up to use the generated C81 tables and predict the rotor performance. The CAMRADII aerodynamic model for the rotor blade is based on lifting-line theory, using steady two-dimensional airfoil characteristics and a vortex wake model, and additional models for unsteady flow (attached flow and dynamic stall) and yawed/swept flow. Effects of compressibility (Mach numbers) and viscosity (Reynolds number, stall, and drag) enter through airfoil table data: lift, drag, and moment coefficients of two-dimensional sections as function of angle of attack and Mach number, for the appropriate chord and atmosphere (density, temperature) to have correct Reynolds number variation with Mach number. In the paper, the term "CA cases" is used to refer to the same rotor model as that indicated by "2D OVERFLOW" or "2D CFD cases".

1. Grid Generation for 2D Airfoils

The Ingenuity airfoil coordinates [9] were interpolated to yield a high density set of coordinates. In contrast to the geometry in Ref. [8], airfoil geometry for all eight radial stations was not based on the original airfoil geometry design, but on the as-built geometry and extracted from the outer mold line (OML) Computer Aided Design (CAD) model. This same geometry is used for the 3D CFD, to allow for a direct comparison. The main difference with the profiles used in Ref. [8] is the constant thickness trailing edge on the actual Ingenuity rotor geometry of around 0.5 mm.

Grids were generated using Chimera Grid Tools 2.2 (CGT) [28] and the gridding guidelines from the American Institute of Aeronautics and Astronautics (AIAA) CFD High Lift Prediction Workshop were used where applicable [29]. The (2D) grid size is based on the grid resolution study (GRS) at $\alpha = 4°$ (approximate outboard angle of attack in hover for Ingenuity [9]) at conditions corresponding to radial stations $r/R = 0.50, 0.75, 0.90$. Through independent halving of the physical time step and doubling the grid density in each coordinate direction, it was ensured that finer grids in space and time resulted in relative changes of the mean integrated aerodynamic coefficients comfortably below 0.1%, while simultaneously ensuring at least 100 timesteps per shedding cycle of the boundary layer. This resulted in an O-grid with chordwise spacing at the leading edge (LE) and trailing edge (TE) set to $0.001\%c$ and $0.01\%c$, respectively. The number of cells over the TE is monitored to ensure adequate gridding. The maximum chordwise separation was fixed at $0.5\%c$ to provide a reasonably uniform chordwise grid spacing in the predominant region of unsteady separated flow.

Simulations are performed between $\alpha = [-15°, 20°]$ in steps of 1 degree for 8 radial stations and 6 Mach numbers on average, resulting in around 5,000 time-accurate airfoil simulations for the three rotor models at the three density conditions.

The viscous wall spacing is estimated for the first point of the airfoil surface at $10\%c$ and kept at $y^+ < 1$ for all Reynolds numbers studied. The initial wall spacing layer contains five layers of constant cell spacing normal to the viscous walls. The cell stretching ratio (SR) for the normal and tangential/chordwise layers is kept at 7% and the farfield is located at $200c$ for all grids. The number of cells normal to the surface is obtained from the target stretching ratios.

The grid is generated to anticipate thick boundary layers and unsteady separated shear layer behavior because of the low Reynolds numbers experienced by the rotor. As such, the maximum chordwise and off-body separation was fixed at $0.5\%c$ in the predominant region of unsteady separated flow, as shown in red in Figure 3.
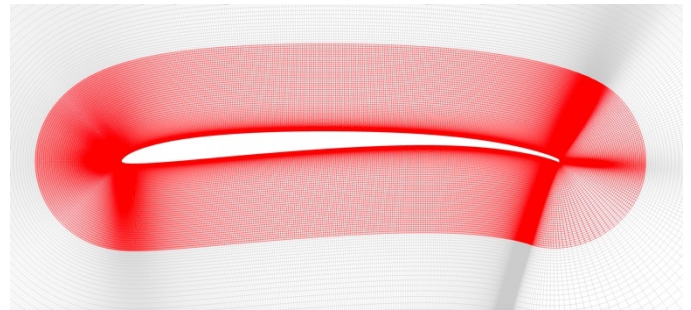

Figure 3 The near body grid for the clf5605 airfoil.

This 'maximum global separation' is constrained up to $0.20c$ normal to the airfoil surface, in order to approach uniformly sized cells in the predominant region where large-scale unsteady flow is expected (red in Figure 3). After $0.20c$ normal to the airfoil surface, the regular hyperbolic stretching is continued while ensuring a smooth transition (grey in Figure 3).

Figure 4 shows the vorticity magnitude around the clf5605 airfoil for expected conditions at a spanwise distance of $r/R = 0.75$ to illustrate the flowfields at different angles of attack. Figure 5 and Figure 6 show increases in angle of attack to 6 and 8 degrees, respectively, showing the vast change in flow structure and complexity. The shear layer instability on the upper surface is clearly seen to progressively move upstream as angle of attack is increased. These large-scale vortical dynamics are key to the performance of airfoils at these conditions.
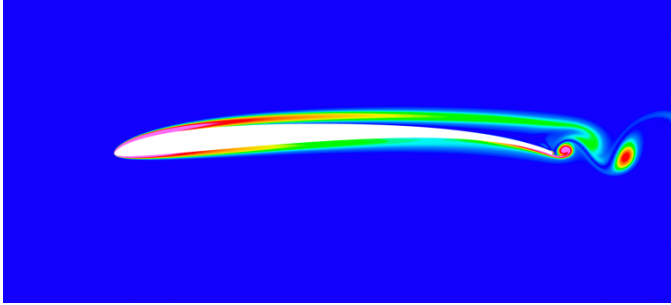
Figure 4 Ingenuity airfoil r/R = 0.75, α = 4°, instantaneous vorticity magnitude.
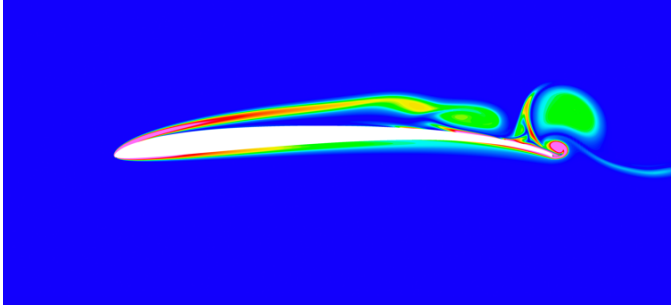
Figure 5 Ingenuity airfoil r/R = 0.75, α = 6°, instantaneous vorticity magnitude.
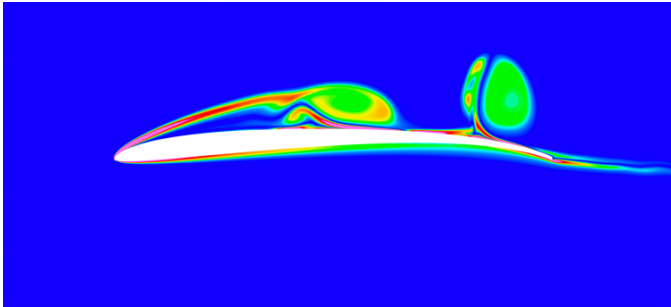
Figure 6 Ingenuity airfoil r/R = 0.75, α = 8°, instantaneous vorticity magnitude.

B. 3D Aerodynamic Rotor Performance Simulations

For a select number of cases, high-fidelity 3D CFD simulations were performed at fixed collective values for the upper and lower rotors. Accurate predictions of FM for high-fidelity 3D rotor simulations operating at higher Reynolds numbers (in fully turbulent flow) are generally observed to require both higher order spatial differencing and adequate turbulence modeling [27,30]. To obtain results within experimental error, the state-of-the-art solution is to use a hybrid RANS/Large Eddy Simulation (LES) model such as the Spalart-Allmaras (SA) turbulence model with a Detached Eddy Simulation (DES) approach: SA-DES [31]. As described above, best practices in modeling turbulence at low Reynolds numbers are not fully defined. The advised SA-DES approach relies on a fully turbulent SA model and is therefore not applicable for low Reynolds number studies. Furthermore, transition modeling, especially in unsteady flows, is still an active field of study in RANS simulations and, therefore, laminar UNS will be evaluated for the current work.

The high-fidelity model uses the same numerical approach as the sectional simulations, but the timestep will be increased and the grid density will be decreased in order to keep the high-fidelity simulations practical. The same airfoil profiles are used to generate the 3D rotor blades, thereby minimizing discrepancies in airfoil geometry along the rotor between the two approaches.

1. Grid Generation for the 3D Rotor

The wake grid resolution and time steps for the 3D hover simulations followed the grid and time step recommendations as described by Ref. [27]. Figure 7 shows the rotor wake grids where the Level 1 (L1) wake grid was defined to enclose the rotors and extends $0.75R$ below the center of the two coaxial rotors with a grid spacing of 0.003m or 6.7% of a tip chord ($c_{tip} = 0.045$), which is below the typical 10% tip chord used for hover performance. Adaptive Mesh Refinement (AMR) was used to capture the rotor wake $2.10R$ below the center of the coaxial rotors using the same L1 wake grid resolution of 0.003m. This resulted in a computational cost savings because the rotor wake is only resolved where needed.
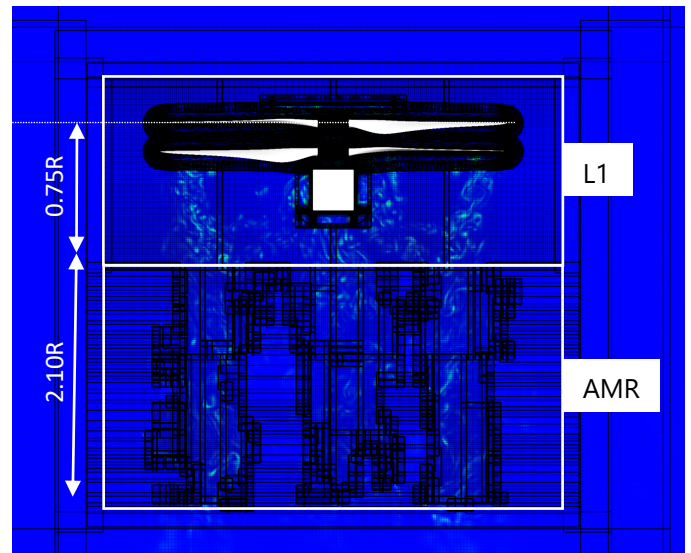

Figure 7 Wake grids for 3D CFD hover calculations for coaxial rotors showing L1 and AMR zones with vorticity magnitude contours.

The coaxial and single rotor simulations were discretized with 15 million grid points per rotor blade with 5 overset grids. The main blade grid consisted of 258 grid points along the span and 401 grid points at each blade station in the chordwise direction and 91 grid points normal to the blade surface. The coaxial rotor simulations had a total of 216 million grid points,

60 million for the rotor body grids, 76 million for the background grids and 80 million for the AMR. The single rotor simulation had a total of 186 million grid points with the same number of background and AMR grids but with 30 million fewer rotor body grids.

2. Timestep and solution procedure for the 3D rotor

A physical time step of ¼-degree blade rotation was used with a 2-order drop in the L_2-norm. The calculations used an adaptive number of subiterations until a 2-order drop in the L_2-norm was achieved. Typically, 13 to 17 subiterations were typically needed to obtain a 2-order drop in the L_2-norm.

A 'quick-start', quasi time-accurate, procedure was used as described by Ref. [27] where a larger time step (1 degree for this investigation) was used with only 1-order of convergence and no AMR. This results in a factor of 10 in cost saving per revolution using the quick-start approach versus the time accurate ¼ degree, 2-order L_2-norm time-accurate simulation. For the coaxial rotor simulations, 40 rotor revolutions were performed using the quick-start approach to establish the rotor wake and remove any transients due to starting the rotor simulations. The simulation was then switched to the time-accurate approach using ¼-degree blade rotation and 2-orders of convergence. The hover simulations at the ¼-degree time stepping were run for a total of 4 revolutions. Figure 8 and Figure 9 shows the convergence of the FM for a coaxial simulation using the quick start procedure for the 15-degree collective for the upper and lower rotor, respectively.
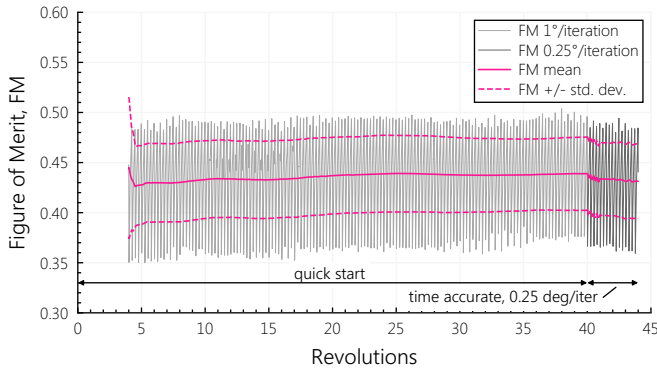
Figure 8 FM convergence using quick-start and time-accurate procedure for coaxial rotor at a collective of 15 degrees showing the upper rotor.

IV. Results

Rotor performance figures are presented for the TRT and EDM1 test results, and 2D and 3D CFD simulations. Due to the high computational cost of the 3D CFD cases, cases near peak FM were prioritized to highlight performance at peak efficiency and the onset of stall. Next, select cases are highlighted to illustrate where the differences between 2D and 3D CFD predictions originate by examining the spanwise distributions of thrust and power. Lastly, the flowfield at $r/R = 0.75$ is compared to illustrate the effect of spanwise flow on the performance.
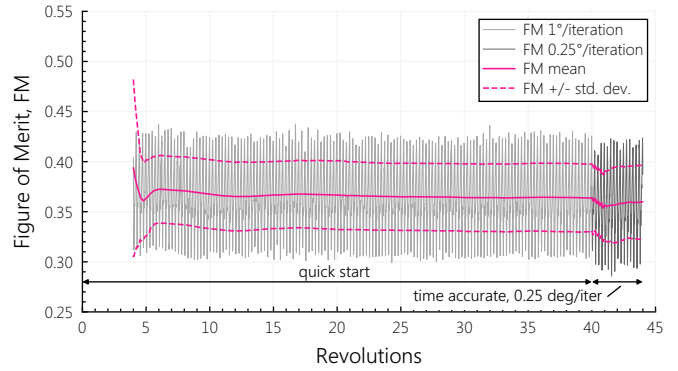
Figure 9 FM convergence using quick-start and time-accurate procedure for coaxial rotor at a collective of 15 degrees showing the lower rotor.

A. Single Rotor Performance and TRT data

An overview for the TRT results is presented for TRT condition 3 ($M_{tip} = 0.75$). Figure 10 presents rotor power versus thrust for the single TRT rotor conditions. The overall agreement is fair until a blade loading of around $C_T/\sigma > 0.15$ where the stall behavior of the computational methods predicts higher efficiencies at stall (onset).
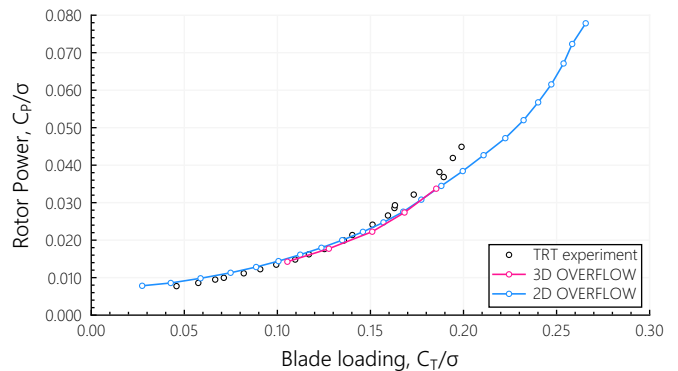

Figure 10 Rotor power versus blade loading for TRT condition 3 ($M_{tip} = 0.75$).

Figure 11 shows the figure of merit distribution for the same dataset. The correlation between 2D CFD and the experimental data is fair until peak FM is reached, albeit at an offset in blade loading. This offset seems to not be present in the 3D CFD results, but the differences in figure of merit at the onset of stall are similar to 2D CFD.

To highlight the predictive capabilities for rotor thrust, the blade loading versus collective angle is presented in Figure 12. The difference in slope between computational and experimental results is clear.
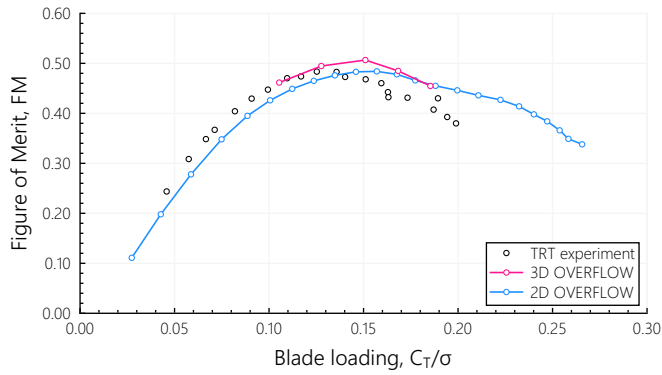
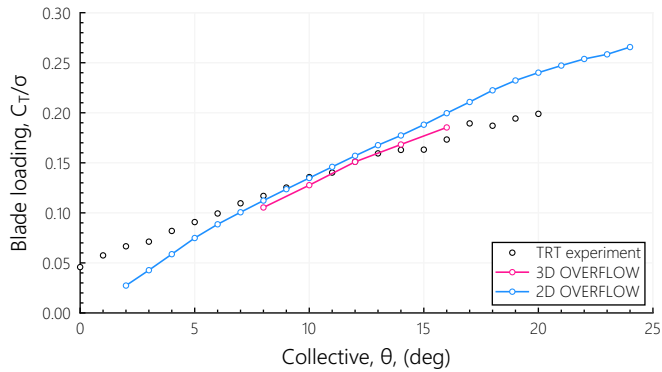**Figure 11 Figure of merit versus blade loading for TRT condition 3 (M_tip = 0.75).**

Figure 12 Blade loading versus collective for TRT condition 3 (M_tip = 0.75).

Figure 13 shows the flowfield at TRT condition 3 ($M_{tip} = 0.75$) for a single rotor at $\theta = 14°$. The Q-criterion isosurface is shown, colored by vorticity magnitude, to highlight the complexity of the flow near the outboard sections of the rotor.
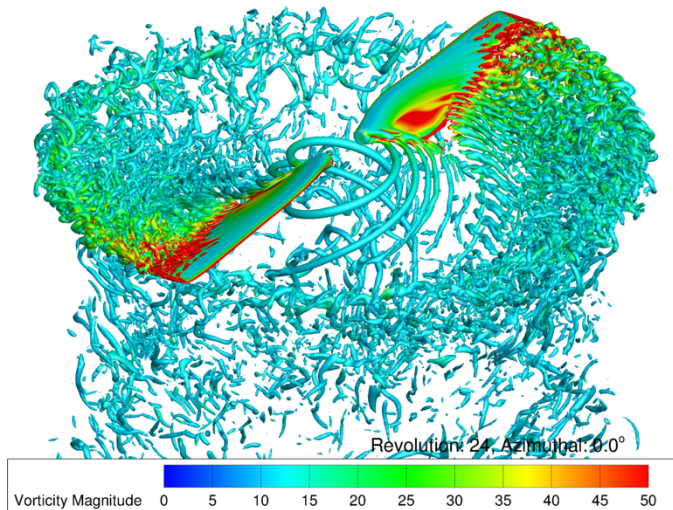

Figure 13 Q-criterion colored by vorticity magnitude, TRT Condition 3, θ = 14°.

B. Coaxial Rotor Performance and EDM1 data

The EDM1 campaign was performed with the Ingenuity Engineering Design Model 1, including the body, solar panel,

and landing legs during the experiment and were part of the measured vehicle thrust. The 2D CFD results did not include a manner to account for the effects of the body, solar panel or landing legs. Most of the 3D CFD simulations were performed without the body, solar panel and landing legs in order to compare directly to the CA results. However, 3D CFD was performed at two collective angles with the body and solar panel to quantify their effect on performance.

Figure 14 presents coaxial rotor power versus thrust at EDM1 condition 1 ($\rho = 0.0100 \, \text{kg/m}^3$). The results show adequate agreement between the computational approaches and, similarly to Figure 10, show increased power mismatch with experimental data at increasingly higher thrust levels.
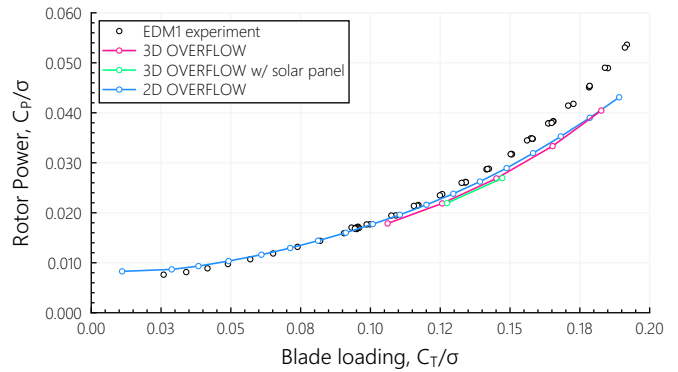
Figure 14 Rotor power versus blade loading for EDM1 condition 1 (ρ = 0.0100 kg/m³).

Figure 15 shows the figure of merit distribution for EDM1 condition 1. 2D CFD results at low blade loading are acceptable but exceed experimental results near peak FM and above. 3D CFD results show slight increases in FM, but with a similar peak FM blade loading.
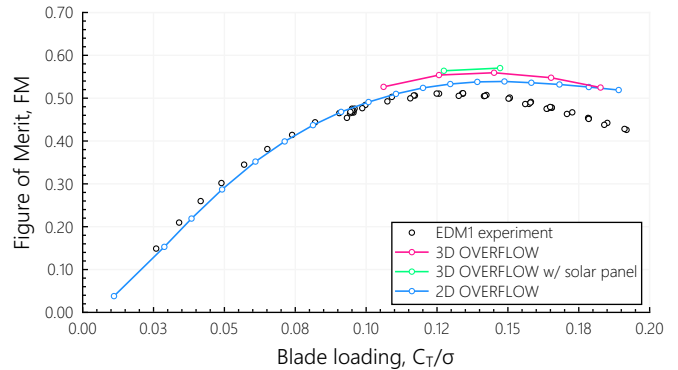
Figure 15 Figure of merit versus blade loading for EDM1 condition 1 (ρ = 0.0100 kg/m³).

Including the solar panel and body in the 3D CFD calculations did result in a 1.0% to 1.2% increase in total thrust of the entire vehicle resulting in a 1.5% increase in FM. The 3D CFD simulations did not include the landing legs, which would increase the download on the vehicle, reducing thrust.

Blade loading versus collective angle is shown in Figure 16 and highlights a similar mismatch in slope between computational and experimental efforts to the TRT results in Figure 12, albeit les pronounced. While the predicted slope is

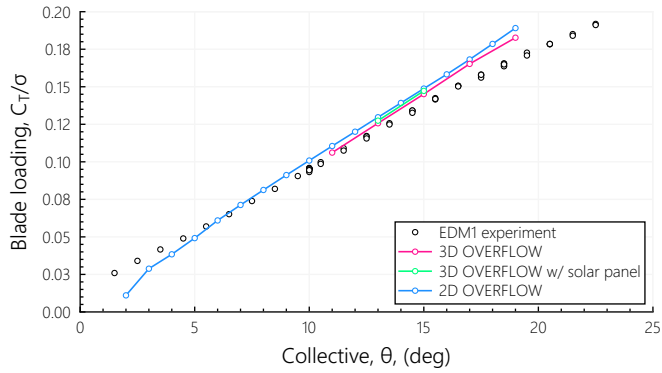similar for the computational approaches, the dissimilarity with the experimental results is evident.

Figure 16 Blade loading versus collective for EDM1 condition 1 ($\rho = 0.0100$ kg/m³).

For the computational results, the coaxial rotor performance can be split into separate predictions for upper and lower rotor performance. Figure 17 shows the same data as Figure 16, but now split per upper and lower rotor. The results present a clear correlation for the lower rotor between the computational data. However, the good lower rotor performance correlation is likely misleading: taking the 3D CFD results as ground truth the increased upper rotor performance from 2D CFD would result in a decreased mean angle of attack over the lower rotor blades. This would roughly correspond to a few percent change in lift coefficient which would in turn make the correlation less favorable.
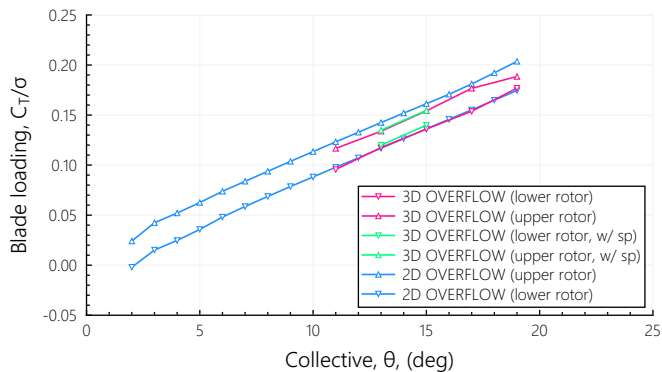
Figure 17 Blade loading versus collective per rotor for EDM1 condition 1 ($\rho = 0.0100$ kg/m3).

Several 3D CFD cases were run for EDM1 condition 4 to evaluate if a change in operating conditions and Reynolds number would change the fundamental correlation challenges to the experimental data. Figure 18 presents coaxial rotor power versus thrust at EDM1 condition 4 ($\rho = 0.0300\,\mathrm{kg/m^3}$) which bears resemblance to the curves for EDM1 condition 1. Figure 19 shows the figure of merit distribution for the same dataset. Overall, the trends of the computational analyses are similar to the results for EDM1 condition 1. The 3D CFD predictions show a lower blade loading for identical collective, but still increased figure of merit compared to the CA cases because of the drop in rotor power.

The blade loading versus collective curves are presented in Figure 20 and show a similar slope between the computational analyses. The narrow thrust range of the EDM1 condition 4 data prevents an exhaustive comparison to experimental data.
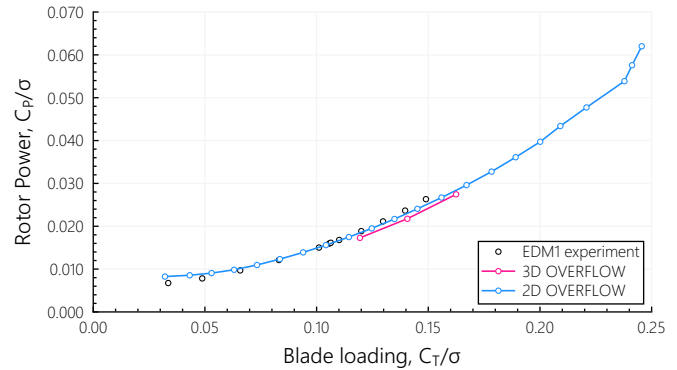
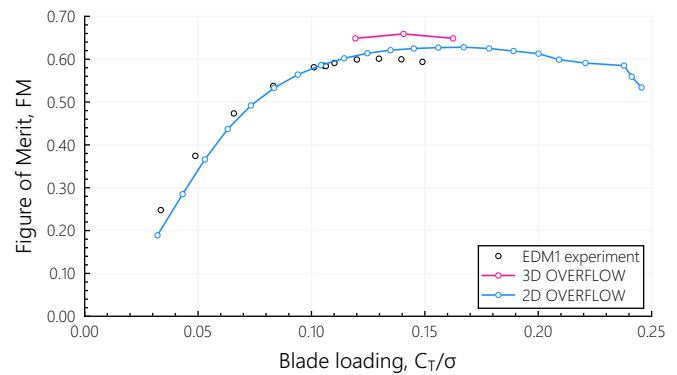**Figure 18 Rotor power versus blade loading for EDM1 condition 4 ($\rho = 0.0300$ kg/m³).**

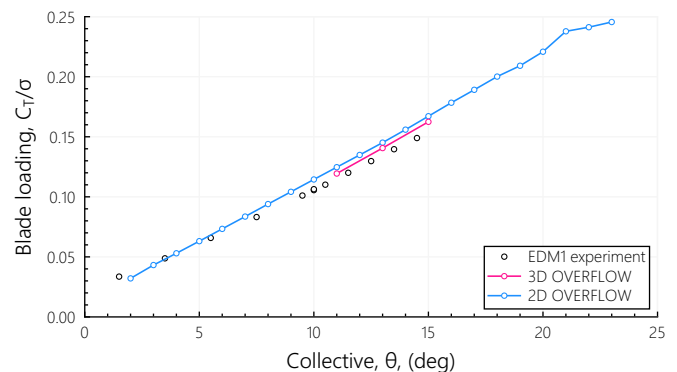**Figure 19 Figure of merit versus blade loading for EDM1 condition 4 ($\rho = 0.0300$ kg/m³).**

Figure 20 Blade loading versus collective for EDM1 condition 4 ($\rho = 0.0300$ kg/m³).

C. TRT Rotor Disk Section Forces

While the agreement between 2D and 3D CFD in sections A and B is favorable, differences are still exceeding desired accuracy. Due to this, further analysis is presented to highlight differences in spanwise loading for select datapoints to pinpoint the origin of the discrepancies across the rotor disk. For the TRT test the collective angles of $\theta = 8°, 14°$ (see Figure 12) are

selected for further analysis, corresponding to pre and post peak FM, respectively. To facilitate direct comparisons, the total thrust from the CA cases was trimmed to that for the 3D CFD cases. Since it is difficult to obtain lift and drag coefficient distributions from 3D CFD (due to the ambiguous value of the angle of attack along the span), the airfoil normal and chord force coefficients are extracted for both computational approaches. Spanwise distributions of thrust and power can then be extracted to examine the origin of thrust and power discrepancies along the span.

1. Case 1: $\theta = 8°, C_T/\sigma = 0.1054$.

Figure 21 shows the (azimuthal-mean) blade thrust distribution for both computational analyses, which highlights a small difference near the tip for case 1. Figure 22 shows the (azimuthal-mean) blade power distribution, showing a difference in power in a more outboard region than the thrust load. The combined thrust and power load clearly illustrate the higher FM of the 3D CFD case for this collective angle, but the overall correlation is fair.
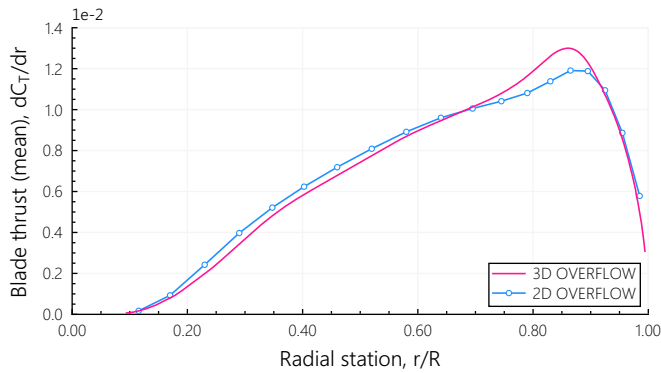
Figure 21 Mean blade thrust distribution, θ = 8°.
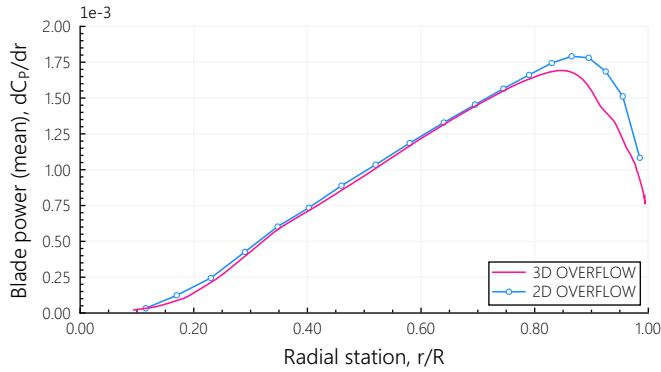
Figure 22 Mean blade power distribution, θ = 8°.

2. Case 2: $\theta = 14°, C_T/\sigma = 0.1683$.

The collective for case 2 is beyond that for peak figure of merit, so as to investigate the correlation for a partially stalled blade. Figure 23 and Figure 24 show a direct comparison of resulting sectional normal and axial (chord) force coefficients versus rotor azimuth for the high thrust case, respectively, for both 3D and 2D CFD. The figures highlight the variation in

blade loading with azimuth that the 3D CFD can capture here, in contrast to the CA.
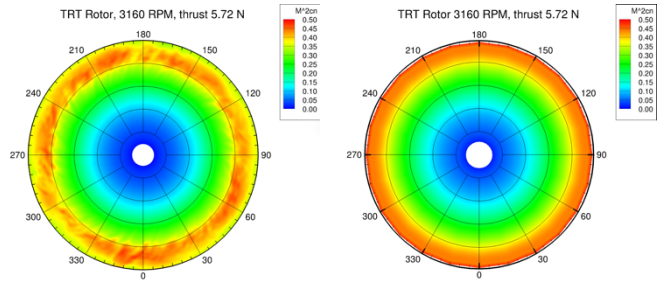

Figure 23 Rotor sectional normal force coefficient for 3D CFD (left) and 2D CFD (right), θ = 14°.

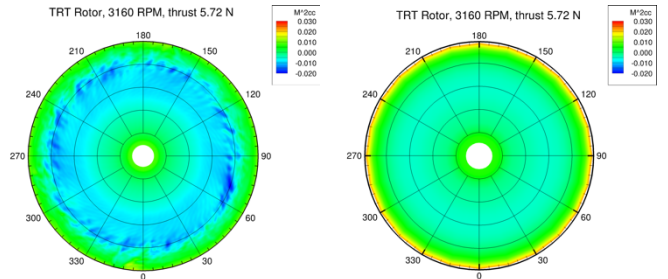**Figure 24 Rotor sectional axial (chord) force coefficient for 3D CFD (left) and 2D CFD (right), θ = 14°.**

Despite the partial stall, the sectional normal force coefficient predictions are qualitatively similar, whereas the sectional axial (chord) force coefficient predictions show unsteady lower inboard forces that are not captured in the 2D CFD.

Figure 25 and Figure 26 show the blade thrust and power distribution, respectively. The distributions show a similar correlation of the blade thrust and power distribution to the lower collective case as shown in Figure 21 and Figure 22, respectively.
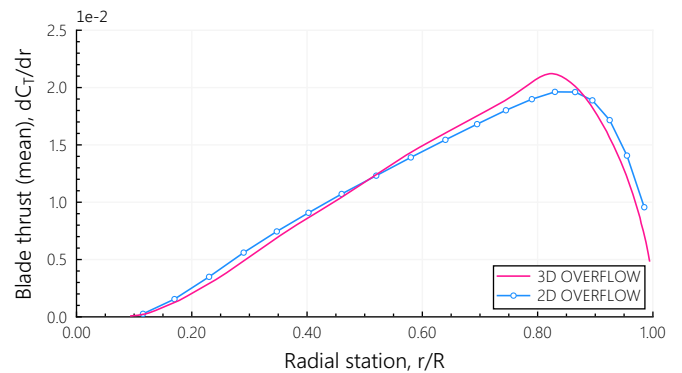

Figure 25 Mean blade thrust distribution, θ = 14°.

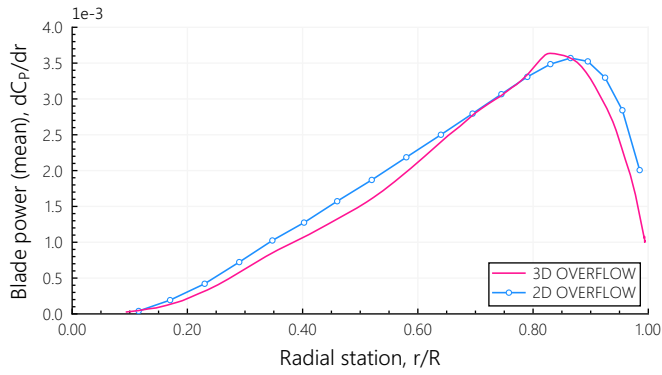**Figure 26 Mean blade power distribution, θ = 14°.**

D. EDM1 Rotor Disk Section Forces

Two collective values for the (coaxial) EDM1 cases are presented to further analyze discrepancies between the computational analyses, in a similar vein to section C showing spanwise load distributions for the TRT conditions. For the EDM1 test the collective angles of $\theta = 15°, 19°$ (Figure 16) are selected for further analysis, corresponding to peak FM and early stall, respectively. To facilitate direct comparisons the total coaxial thrust from the CA cases was trimmed to that for the 3D CFD cases.

1. Case 1: $\theta = 15°, C_T/\sigma = 0.1451$.

Figure 27 and Figure 28 show the sectional normal force coefficients for case 1 for the lower and upper rotor, respectively. Qualitatively, an agreement in azimuthal variation of the normal load is shown.
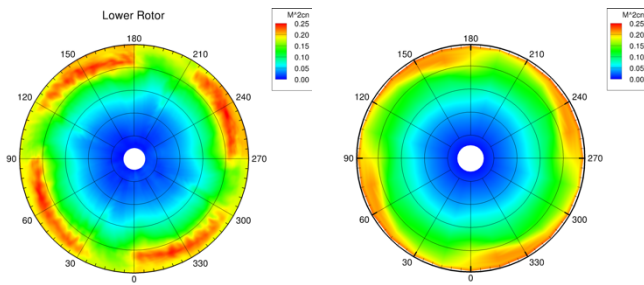
Figure 27 Lower rotor sectional normal force coefficient for 3D CFD (left) and 2D CFD (right), θ = 15°.
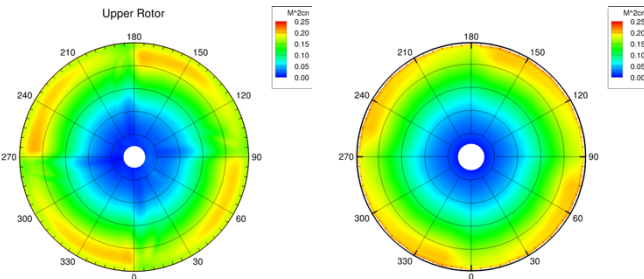
Figure 28 Upper rotor sectional normal force coefficient for 3D CFD (left) and 2D CFD (right), θ = 15°.

The instantaneous blade thrust distribution for the lower and upper rotor is shown in Figure 29 and Figure 30, respectively.

The cases highlight the relatively good agreement between the computational approaches for a coaxial configuration.
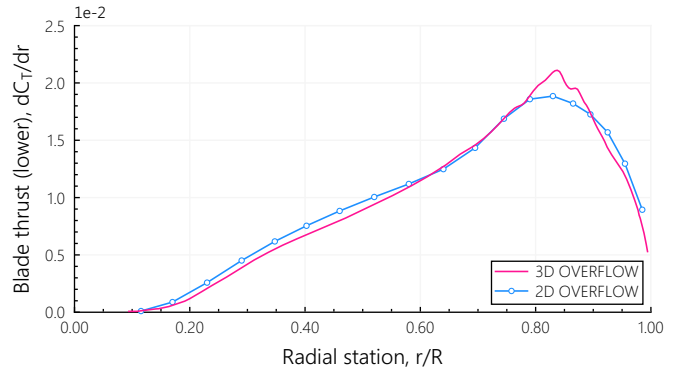

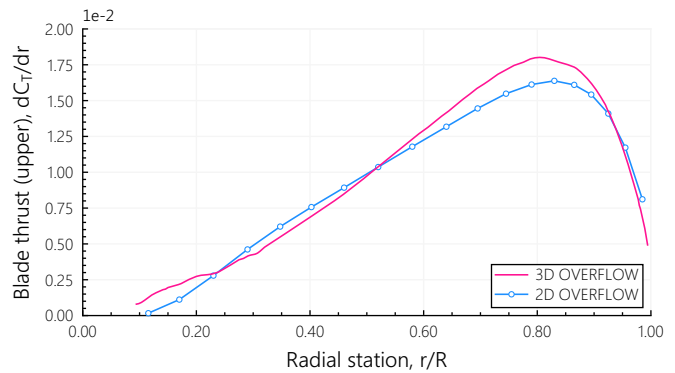**Figure 29 Instantaneous blade thrust distribution, Ψ=90°, θ = 15°, lower rotor.**

Figure 30 Instantaneous blade thrust distribution, Ψ=270°, θ = 15°, upper rotor.

The agreement for the sectional axial (chord) forces is less favorable, showing an unsteady component in the 3D CFD cases for both lower and upper rotor, as shown in Figure 31 and Figure 32, respectively. Azimuthal variations are present in the 2D CFD cases in Figure 31 and Figure 32, but with much lower magnitudes, and therefore less pronounced compared to their 3D CFD counterparts, due to the forced normalization between both computational analyses.
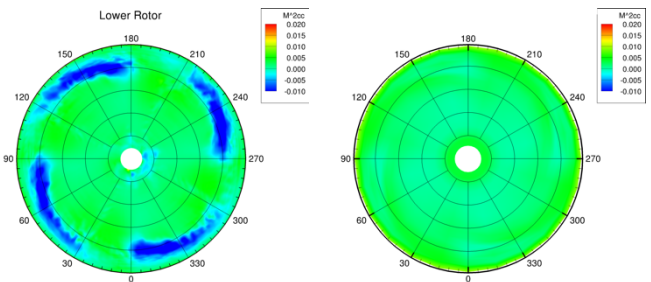

Figure 31 Lower rotor sectional axial (chord) force coefficient for 3D CFD (left) and 2D CFD (right), θ = 15°.

The instantaneous blade power distribution for the lower and upper rotor is shown in Figure 33 and Figure 34, respectively. The lower rotor agreement is fair but is overshadowed by the mismatch across the span for the upper

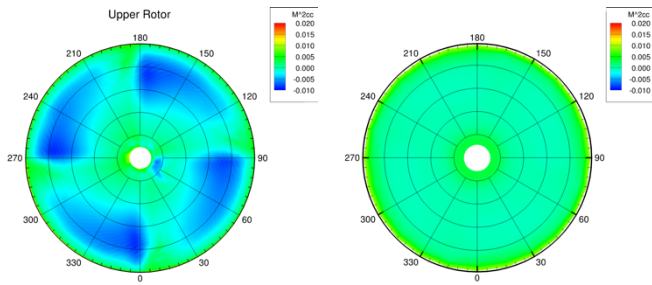rotor, which shows a strong power offset between the analyses across the blades.

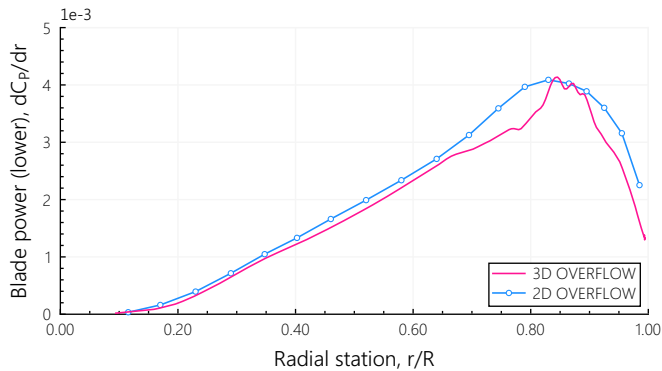**Figure 32 Upper rotor sectional axial (chord) force coefficient for 3D CFD (left) and 2D CFD (right), θ = 15°.**

Figure 33 Instantaneous blade power distribution, Ψ=90°, θ = 15°, lower rotor.
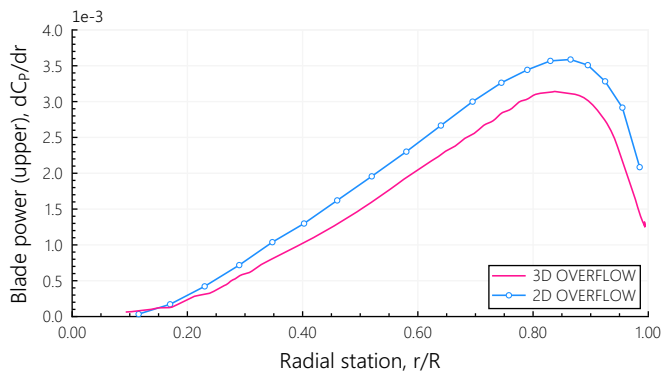
Figure 34 Instantaneous blade power distribution, Ψ=270°, θ = 15°, upper rotor.

2. Case 2: $\theta = 19°, C_T/\sigma = 0.1827$.

Figure 35 and Figure 36 show the sectional normal force coefficients for case 2 for the lower and upper rotor, respectively. The qualitative agreement in azimuthal variation of the sectional normal force coefficient is reasonable, but the upper rotor shows a lower overall force.

The instantaneous blade thrust distribution for lower and upper rotor is shown in Figure 37 and Figure 38, respectively. The lower rotor agreement is adequate, though the upper rotor thrust shows the thrust rapidly climbing towards the tip and then dropping off after about $r/R = 0.65$ as the outboard section of the upper rotor begins to stall. The strong unsteadiness (as

illustrated by the discontinuity of the 3D CFD curves near the tip) further illustrates the distinct differences in predicted aerodynamic environment between the analyses.
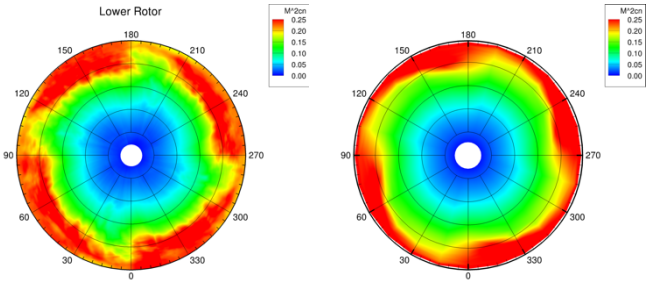

Figure 35 Lower rotor sectional normal force coefficient for 3D CFD (left) and 2D CFD (right), θ = 19°.

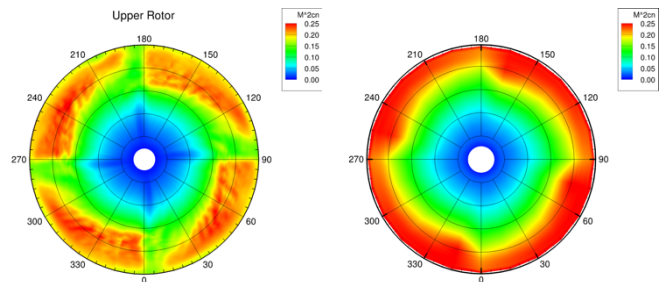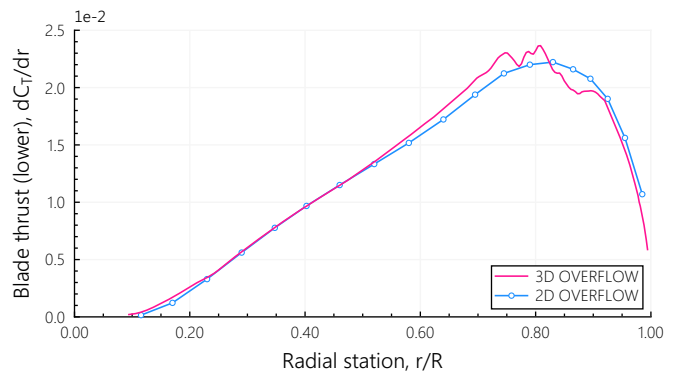**Figure 36 Upper rotor sectional normal force coefficient for 3D CFD (left) and 2D CFD (right), θ = 19°.**

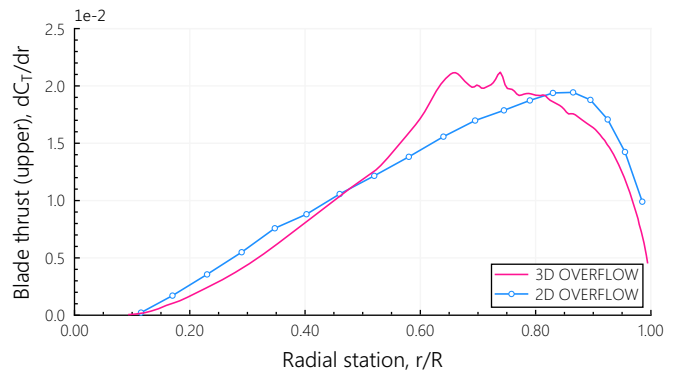**Figure 37 Instantaneous blade thrust distribution, Ψ=90°, θ = 19°, lower rotor.**

Figure 38 Instantaneous blade thrust distribution, Ψ=270°, θ = 19°, upper rotor.

Figure 39 and Figure 40 show the sectional axial (chord) force coefficients for case 2 for the lower and upper rotor, respectively. Both rotors show significantly lower airfoil chord forces for the 3D CFD case, compared to the CA (2D CFD) case.
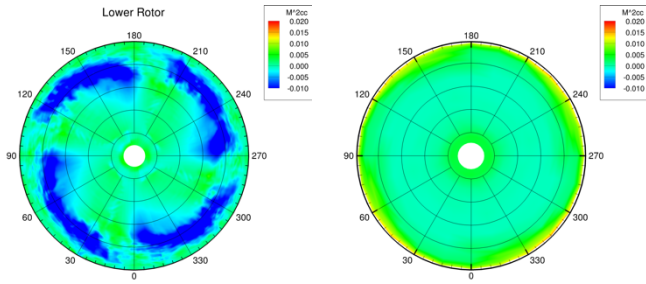

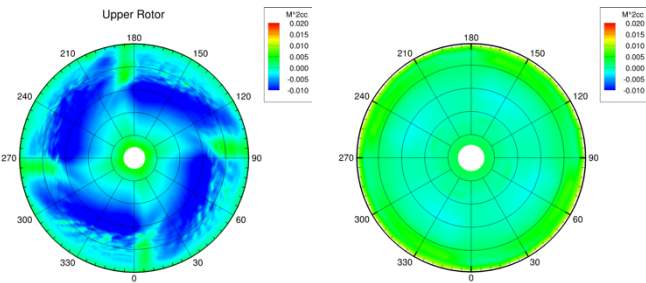**Figure 39 Lower rotor sectional axial (chord) force coefficient for 3D CFD (left) and 2D CFD (right), θ = 19°.**

Figure 40 Upper rotor sectional axial (chord) force coefficient for 3D CFD (left) and 2D CFD (right), θ = 19°.

The instantaneous blade power distribution for the lower and upper rotor is shown in Figure 41 and Figure 42, respectively. The upper rotor stall in the 3D CFD case is visible here as the outboard section power ($r/R \gtrsim 0.70$) starts to become very unsteady near the tip, directly correlated to the discontinuities observed for the corresponding thrust distributions in Figure 37 and Figure 38.
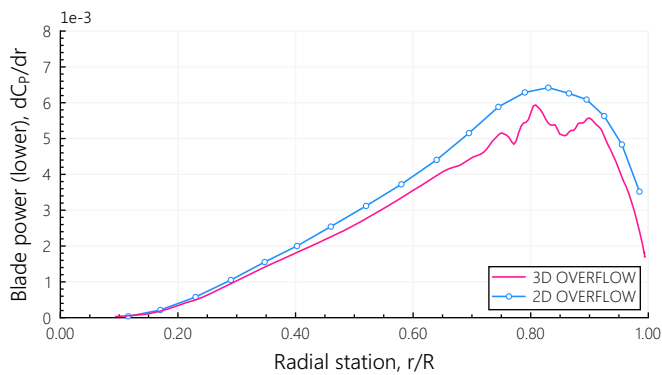

Figure 41 Instantaneous blade power distribution, Ψ=90°, θ = 19°, lower rotor.

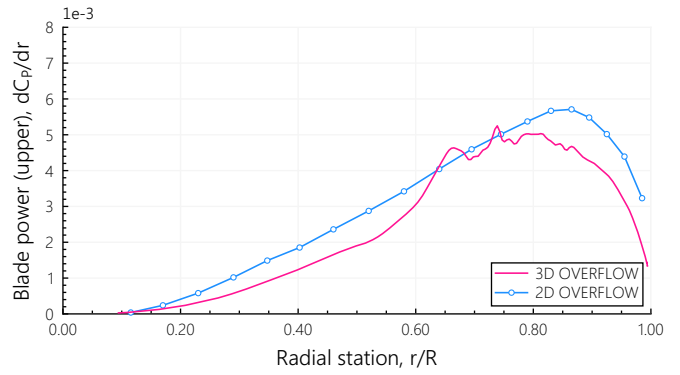**Figure 42 Instantaneous blade power distribution, Ψ=270°, θ = 19°, upper rotor.**

E. Influence of Spanwise Flow

One key difference between the 3D CFD and CA analyses is the existence of spanwise flow in fluid dynamics input of the former. Figure 43 shows the Q-criterion iso-surface colored by vorticity magnitude for a TRT case at $\theta = 16°$.
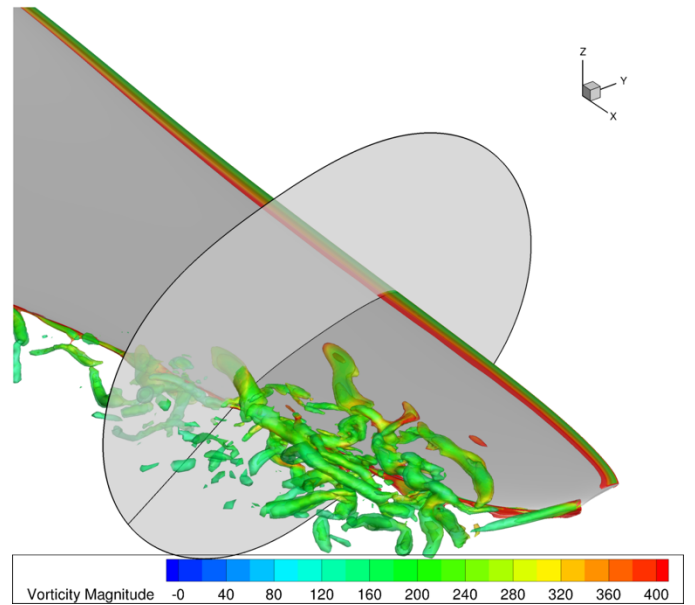
Figure 43 Q-criterion color by vorticity magnitude for TRT condition 1, θ = 16° (slice at r/R = 0.75).

A slice at $r/R = 0.75$ (perpendicular to the pitch axis) is shown too. Figure 44 shows the flowfield as velocity magnitude (normalized by freestream) at the slice for the 2D CFD (left) and the equivalent location in 3D CFD. This highlights the strong influence of the spanwise component on the local flowfield, and hence the aerodynamic performance predictions of the blade. However, when the spanwise components are removed from the 3D CFD flowfield, the flowfields are qualitatively similar, as shown in Figure 45.

Figure 44 Instantaneous velocity magnitude at r/R = 0.75 for 2D CFD (left) and 3D CFD (right), TRT, θ = 16°.

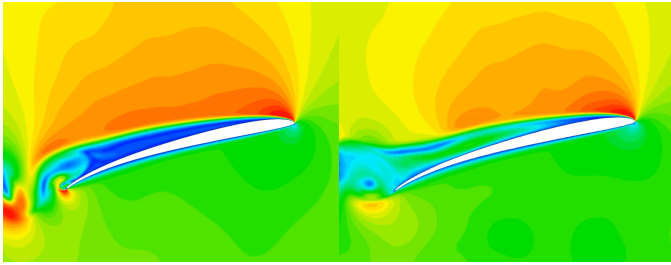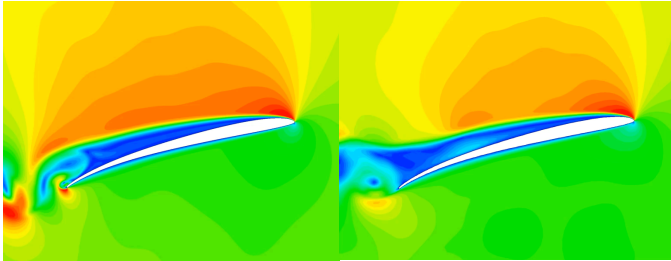**Figure 45 Instantaneous velocity magnitude, spanwise component removed, at r/R = 0.75 for 2D CFD (left) and 3D CFD (right), TRT, θ = 16°.**

V. Discussion

The reason for the differences between experimental and computational results presented remains inconclusive at this point. The 2D CFD analyses of airfoils will show differences to finite-width airfoil simulations [26], though this does not explain why the slopes of the CA and 3D-based CFD simulations for blade loading as function of collective look similar for both the single and coaxial rotor predictions in Figure 12 and Figure 16. Despite differences that could be attributed due to the large difference in computational fidelity, 3D CFD and CA cases (2D CFD) are showing similar trends in the figures presented in Sections A and B. A future study may also be performed in order to quantify the effect of the landing legs on the total vehicle thrust and hover performance.

A. Modeling of Small-scale Turbulence

Differences in FM predictions between 2D and 3D CFD are due to differences in fidelity of the CFD efforts. One possible source of inaccuracy of the computational analyses is the modeling of small-scale turbulence. However, recent work has demonstrated the airfoil simulations with unsteady laminar separation bubbles can be modeled accurately using the current numerical approach at much higher Reynolds numbers [26], albeit with the inclusion of spanwise flow. A strong source of small-scale turbulence at much lower Reynolds numbers considered here is deemed unlikely at low to moderate angles of attack.

B. Spanwise Distributions

A further look into the spanwise distributions suggests that 3D CFD predicts strong unsteadiness near the blade tips post peak FM in contrast to the CA cases (2D CFD). Part of the reduced unsteadiness in the CA cases is readily explained as the

CA analyses rely on C81 tables with mean flow values for the aerodynamic coefficients, but the 2D sectional stall predictions and/or the 3D flowfield around the blade are seen to alter the flowfield around the outer regions of the blade. The flowfield comparison at $r/R = 0.75$ illustrates that removal of the spanwise component in 3D CFD resembles the flowfield of the strictly 2D simulations. This could point to the 3D flow around the blade being the primary reason for differences in aerodynamic flow, rather than the strict 2D assumption in the CA case 2D CFD input tables.

VI. Conclusions

High-fidelity 3D CFD is used for performance predictions of the isolated Ingenuity rotor and compared to CA based on 2D CFD airfoil lookup tables. Computational analyses are presented for single and coaxial rotor setups and are compared to experimental single and coaxial rotor performance data at representative Mars conditions.

Rotor performance metrics are compared and show reasonable agreement between the computational analyses. Correlation with experimental data shows consistent discrepancies at high blade loading (near or post peak figure of merit) and shows a consist change in blade loading slope with rotor collective angle. The reason for the differences in rotor performance predictions between computational and experimental approaches is currently not known.

Analyses of the spanwise distributions of thrust and power show differences in stall, which first become apparent at the outboard sections of the blade. Comparisons at lower collective angles generally shows favorable agreement of blade thrust and power distributions with differences likely attributable to the significant differences in fidelity of the computational approaches.

References

[1]   Balaram, J. (Bob), Canham, T., Duncan, C., Golombek, M., Grip, H. F., Johnson, W., Maki, J., Quon, A., Stern, R., and Zhu, D., "Mars Helicopter Technology Demonstrator," AIAA Science and Technology Forum and Exposition (AIAA SciTech), AIAA Paper 2018-0023, January 2018. https://doi.org/10.2514/6.2018-0023.

[2]   Pipenberg, B. T., Keennon, M., Tyler, J., Hibbs, B., Langberg, S., Balaram, J., Grip, H. F., and Pempejian, J. "Design and Fabrication of the Mars Helicopter Rotor, Airframe, and Landing Gear Systems." AIAA

Science and Technology Forum and Exposition (AIAA SciTech), AIAA Paper 2019-0620, January 2019. https://doi.org/https://doi.org/10.2514/6.2019-0620.

[3] Pipenberg, B. T., Keennon, M. T., Langberg, S. A., and Tyler, J. D. "Development of the Mars Helicopter Rotor System." Vertical Flight Society 75th Annual Forum, Philadelphia, PA, May 2019.

[4] Grip, H. F., Johnson, W., Malpica, C., Scharf, D. P., Mandić, M., Young, L., Allan, B., Mettler, B., and Martin, M. S. "Flight Dynamics of a Mars Helicopter." 43rd European Rotorcraft Forum, 2017, September 2017.

[5] Grip, H. F., Scharf, D. P., Malpica, C., Johnson, W., Mandic, M., Singh, G., and Young, L. A. "Guidance and Control for a Mars Helicopter." AIAA Guidance, Navigation, and Control Conference, AIAA Paper No. 2018-1849, January 2018. https://doi.org/https://doi.org/10.2514/6.2018-1849.

[6] Grip, H. F., Lam, J., Bayard, D. S., Conway, D. T., Singh, G., Brockers, R., Delaune, J. H., Matthies, L. H., Malpica, C., and Brown, T. L. "Flight Control System for NASA's Mars Helicopter." AIAA Science and Technology Forum and Exposition (AIAA SciTech), AIAA Paper 2019-1289, January 2019. https://doi.org/https://doi.org/10.2514/6.2019-1289.

[7] Grip, H. F., Johnson, W., Malpica, C., Scharf, D. P., Mandić, M., Young, L., Allan, B., Mettler, B., Martin, M. S., and Lam, J. "Modeling and Identification of Hover Flight Dynamics for NASA's Mars Helicopter." *Journal of Guidance, Control, and Dynamics*, Vol. 43, No. 2, February 2020. https://doi.org/10.2514/1.G004228.

[8] Koning, W. J. F., Johnson, W., and Grip, H. F. "Improved Mars Helicopter Aerodynamic Rotor Model for Comprehensive Analyses." *AIAA Journal*, Vol. 57, No. 9, September 2019. https://doi.org/10.2514/1.J058045.

[9] Koning, W. J. F., Johnson, W., and Allan, B. G. "Generation of Mars Helicopter Rotor Model for Comprehensive Analyses" American Helicopter Society Technical Conference on Aeromechanics Designs for Transformative Vertical Flight, San Francisco, CA, January 2018.

[10] Young, L. A. "Vertical Lift - Not Just for Terrestrial Flight." American Helicopter Society International Powered Lift Conference, Crystal City, VA, October 2000.

[11] Young, L. A., and Aiken, E. W. "Vertical Lift Planetary Aerial Vehicles: Three Planetary Bodies and Four Conceptual Design Cases." 27th European Rotorcraft Forum, 2001, Moscow, Russia, September 2001.

[12] Young, L. A., Aiken, E. W., Derby, M., Demblewski, R., and Navarrete, J. "Experimental Investigation and Demonstration of Rotary-Wing Technologies for Flight in the Atmosphere of Mars." American Helicopter Society 58th Annual Forum, Montreal, Canada, June 2002.

[13] Young, L. A., Aiken, E. W., Gulick, V., Mancinelli, R., and Briggs, G. A. "Rotorcraft as Mars Scouts." IEEE Aerospace Conference, 2002, Big Sky, MT, March 2002.

[14] Datta, A., Roget, B., Griffiths, D., Pugliese, G., Sitaraman, J., Bao, J., Liu, L., and Gamard, O. "Design of a Martian Autonomous Rotary-Wing Vehicle." *Journal of Aircraft*, Vol. 40, No. 3, May-June 2003. https://doi.org/10.2514/2.3141.

[15] Balaram, J., and Tokumaru, P. T. "Rotorcrafts for Mars Exploration." 11th International Planetary Probe Workshop, Pasadena, CA, 2014.

[16] Mier-Hicks, F., Grip, H. F., Kalantari, A., Moreland, S., Pipenberg, B., Keennon, M., Canham, T. K., Pauken, M., Decrossas, E., and Tzanetos, T. "Sample Recovery Helicopter." 2023 IEEE Aerospace Conference, Big Sky, MT, USA, 2023. doi: 10.1109/AERO55745.2023.10115951.

[17] Drela, M., and Youngren, H. "XROTOR: An Interactive Program for the Design and Analysis of Ducted and Free-Tip Propellers and Windmills." https://web.mit.edu/drela/Public/web/xrotor/xrotor_doc.txt, November 2003.

[18] Johnson, W. "Rotorcraft Aerodynamics Models for a Comprehensive Analysis." AHS International 54th Annual Forum & Technology Display, Fairfax, VA, 1998.

[19] Johnson, W. "Influence of Lift Offset on Rotorcraft Performance." NASA TP 2009-215404, 2009.

[20] Nichols, R. H., and Buning, P. G. "User's Manual for OVERFLOW 2.2." Langley Research Center, Hampton, VA, 2008

[21] Pulliam, T. H., "High Order Accurate Finite-Difference Methods: As Seen in OVERFLOW." 20th AIAA Computational Fluid Dynamics Conference, AIAA Paper 2011-3851, June 2011.

[22] Tramel, R., Nichols, R., and Buning, P., "Addition of Improved Shock-Capturing Schemes to OVERFLOW 2.1." 19th AIAA Computational Fluid Dynamics, AIAA Paper 2009-3988, June 2009.

[23] Pulliam, T. H. "Time Accuracy and the Use of Implicit Methods." AIAA Computational Fluid Dynamics Conference, AIAA Paper 1993- 3360, July 1993. https://doi.org/10.2514/6.1993-3360.

[24] Pandya, S., Venkateswaran, S., and Pulliam, T. H. "Implementation of Preconditioned Dual-Time Procedures in OVERFLOW." AIAA 41st Aerospace Sciences Meeting, AIAA Paper 2003-0072, Jan. 2003. https://doi.org/10.2514/6.2003-72.

[25] Coder, J. G., Pulliam, T. H., and Jensen, J. C. "Contributions to HiLiftPW-3 Using Structured, Overset Grid Methods." 2018 AIAA Aerospace Sciences Meeting, AIAA Paper 2018-1039, January 2018. https://doi.org/10.2514/6.2018-1039

[26] Koning, W. J. F., Romander, E. A., Cummings, H. V., Perez Perez, B. N., and Buning, P. G. "On Improved Understanding of Airfoil Performance Evaluation Methods at Low Reynolds Numbers." *Journal of Aircraft*, Vol. 60, No. 3, May 2023. https://doi.org/10.2514/1.C037023

[27] Chaderjian, N. M. "Quantitative Approach for the Accurate CFD Simulation of Hover in Turbulent Flow." International Conference on Computational Fluid Dynamics, Maui, HI, July 2022.

[28] Chan, W. M., Rogers, S. E., Nash, S. M., Buning, P. G., Meakin, R. L., Boger, D. A., and Pandya, S. "Chimera Grid Tools User's Manual, Version 2.0." NASA Ames Research Center, 2007.

[29] Rumsey, C. L., Slotnick, J. P., and Sclafani, A. J. "Overview and Summary of the Third AIAA High Lift Prediction Workshop." AIAA Aerospace Sciences Meeting, AIAA Paper 2018-1258, January 2018. https://doi.org/10.2514/6.2018-1258

[30] Chaderjian, N. M., and Buning, P. G., "High Resolution Navier-Stokes Simulation of Rotor Wakes." Vertical Flight Society 67th Annual Forum, Virginia Beach, VA, May 2011.

[31] Spalart, P., and Allmaras, S. A., "One-Equation Turbulence Model for Aerodynamic Flows." 30th AIAA Aerospace Sciences Meeting and Exhibit, AIAA Paper 1992-439, August 1992. https://doi.org/10.2514/6.1992-439